

Full Length Article



3D osteocyte lacunar morphometry of human bone biopsies with high resolution microCT: From monoclonal gammopathy to newly diagnosed multiple myeloma

Inés Moreno-Jiménez^{a,*}, Sharen Heinig^a, Unai Heras^{b,c}, Daniela Simone Maichl^d, Susanne Striffler^d, Ellen Leich^{e,f}, Stéphane Blouin^g, Peter Fratzl^a, Nadja Fratzl-Zelman^g, Franziska Jundt^{d,f,*,1}, Amaia Cipitria^{a,b,h,*,1}

^a Max Planck Institute of Colloids and Interfaces, Department of Biomaterials, 14476 Potsdam, Germany

^b Group of Bioengineering in Regeneration and Cancer, Biogipuzkoa Health Research Institute, 20014 San Sebastian, Spain

^c Department of Cell Biology and Histology, Faculty of Medicine and Nursing, University of the Basque Country UPV/EHU, 48940 Leioa, Spain

^d Department of Internal Medicine II, University Hospital Würzburg, 97080 Würzburg, Germany

^e Institute of Pathology, University of Würzburg, 97080 Würzburg, Germany

^f Comprehensive Cancer Center Mainfranken, 97080 Würzburg, Germany

^g Ludwig Boltzmann Institute of Osteology at the Hanusch Hospital of OEGK and AUVA Trauma Centre Meidling, Vienna, Austria

^h IKERBASQUE, Basque Foundation for Science, 48009 Bilbao, Spain

ARTICLE INFO

Keywords:

Osteocyte lacuna
Morphometry
High resolution microCT
Human bone biopsy
Multiple myeloma (MM)
Monoclonal gammopathy of undetermined significance (MGUS)
Smoldering multiple myeloma (SMM)

ABSTRACT

Osteocytes are mechanosensitive, bone-embedded cells which are connected via dendrites in a lacuno-canalicular network and regulate bone resorption and formation balance. Alterations in osteocyte lacunar volume, shape and density have been identified in conditions of aging, osteoporosis and osteolytic bone metastasis, indicating patterns of impaired bone remodeling, osteolysis and disease progression. Osteolytic bone disease is a hallmark of the hematologic malignancy multiple myeloma (MM), in which monoclonal plasma cells in the bone marrow disrupt the bone homeostasis and induce excessive resorption at local and distant sites. Qualitative and quantitative changes in the 3D osteocyte lacunar morphometry have not yet been evaluated in MM, nor in the precursor conditions monoclonal gammopathy of undetermined significance (MGUS) and smoldering multiple myeloma (SMM). In this study, we characterized the osteocyte lacunar morphology in trabecular bone of the iliac crest at the ultrastructural level using high resolution microCT in human bone biopsy samples of three MGUS, two SMM and six newly diagnosed MM. In MGUS, SMM and MM we found a trend for lower lacunar density and a shift towards larger lacunae with disease progression (higher 50 % cutoff of the lacunar volume cumulative distribution) in the small osteocyte lacunae 20–900 μm^3 range compared to control samples. In the larger lacunae 900–3000 μm^3 range, we detected significantly higher lacunar density and microporosity in the MM group compared to the MGUS/SMM group. Regarding the shape distribution, the MGUS/SMM group showed a trend for flatter, more elongated and anisotropic osteocyte lacunae compared to the control group. Altogether, our findings suggest that osteocytes in human MM bone disease undergo changes in their lacunae density, volume and shape, which could be an indicator for osteolysis and disease progression. Future studies are needed to understand whether alterations of the lacunae architecture affect the mechanoresponsiveness of osteocytes, and ultimately bone adaptation and fracture resistance in MM and its precursors conditions.

* Corresponding authors.

E-mail addresses: inesmorenojimenez@gmail.com (I. Moreno-Jiménez), jundt_f@ukw.de (F. Jundt), amaia.cipitria@mpikg.mpg.de, amaia.cipitriasagardia@biogipuzkoa.eus (A. Cipitria).

¹ These authors contributed equally to this work.

<https://doi.org/10.1016/j.bone.2024.117236>

Received 19 April 2024; Received in revised form 26 July 2024; Accepted 13 August 2024

Available online 14 August 2024

8756-3282/© 2024 The Authors. Published by Elsevier Inc. This is an open access article under the CC BY-NC license (<http://creativecommons.org/licenses/by-nc/4.0/>).

1. Introduction

Osteocytes are bone-embedded cells, connected via dendrites in a lacuno-canalicular network (LCN). They act as local sentinels in response to external stimuli and regulate the balance between bone resorption/formation [1]. In response to mechanical strain, osteocytes orchestrate the remodeling of the perilacunar bone matrix and thereby change shape and size of their lacunae [2]. Lacunar volume, shape and density were influenced by changes of the surrounding environment, either mechanically or chemically, and by aging or disease. Changes in lacuna volume were observed after exposing mice to non-gravity [3] or after treatment with glucocorticoid slowing down bone metabolism [4], resulting in both cases in larger lacunae. In contrast, smaller lacunar size and lacunar density were observed in rodent models of aging [5] and osteoporosis, where the effect of different anti-resorptive drugs in intracortical microporosities was evaluated [6]. In humans, a decline in lacunar density was observed with aging, while a significantly higher density was found in osteoporotic bone compared to controls [7]. A recent study with human bone biopsy samples of healthy individuals across the life span revealed decreasing osteocyte lacunae density and porosity with aging, before the peak bone mass at 30 years, which then stabilized or even increased after this age [8]. Furthermore, mineralized osteocyte lacunae (micropetrosis) were found increased with aging and osteoporosis, which was attributed to osteocyte apoptosis and improved with bisphosphonates treatment [9]. Changes in lacunar shape, notably becoming smaller and more spherical with age, were linked to aging, resulting in diminished local bone tissue strains, impacting bone mechanosensitivity and fracture resistance [2,10]. Noteworthy, abnormal morphological features were also detected in a large-scale assessment of adolescent idiopathic scoliosis, using high resolution microCT [11].

In cancer, osteocytes, as well as osteoblasts and osteoclasts, communicate with tumor cells and this generates a microenvironment that supports cancer cell growth and stimulates bone destruction [12]. Interactions between breast and prostate cancer cells and osteocytes influenced cancer cell migration and invasion potential and contributed to the establishment and progression of bone metastasis [13,14]. Also, breast cancer cells induced osteocyte apoptosis and altered osteocyte function [15]. Recently, a study of osteotropic cancers in rodents revealed that the spatial distribution of cortical bone microporosity, osteocyte lacunae volume and the LCN characteristics were influenced by the presence of tumor cells in osteolytic lesions [16]. Taken together, changes in the volume and shape of osteocyte lacunae are an indicator of osteolysis in bone metastasis of osteotropic cancers.

An example of an incurable malignancy of the bone marrow and bone is multiple myeloma (MM), in which plasma cells producing monoclonal immunoglobulins disrupt the bone homeostasis towards excessive bone resorption [17]. MM cells alter the bone marrow environment by releasing signals that promote osteoclast activity, while inhibiting osteoblast function [18,19]. There is evidence that MM cells also target osteocytes by enhancing apoptosis and expression of sclerostin, an inhibitor of bone formation [20]. Even though MM cells directly interact with osteocytes and vice versa, the consequences of these interactions on the local bone microstructure are largely unknown [20].

In the clinical setting, two pre-symptomatic stages precede MM: (i) an initial phase named monoclonal gammopathy of underdetermined significance (MGUS), which can progress in (ii) smoldering multiple myeloma (SMM). Both MGUS and SMM patients do not present MM clinical symptoms (CRAB symptoms of MM: hypercalcemia, renal insufficiency, anemia and/or osteolytic bone lesions [21]). In patients with MM, low-dose whole body computed tomography (CT) scans are routinely used to detect osteolytic lesions and fractures [22]. It remains, however, poorly understood whether bone microstructural changes precede the osteolytic lesions.

To identify associations between changes in the bone micro-architecture and fractures, x-ray absorptiometry measuring bone density

or low-dose CT scans were used in two clinical studies [23,24]. In one study, low-dose CT scans showed reduced radiodensity, trabecular thickening and vertebral fractures, demonstrating that focal skeletal changes were significantly associated with further skeletal damages [23]. Some earlier studies had attempted to study bone trabecular thickness and separation in MM patients; however, the resolution limit of clinical CT scans was an obstacle for this objective [25,26]. Our group used advanced imaging techniques (high resolution microCT, synchrotron phase contrast-enhanced microCT, confocal laser scanning microscopy) to evaluate the bone microstructure in an early MM mouse model [27]. We showed irregular shaped osteocyte lacunae, altered osteocyte LCN characteristics and local alterations of the extracellular matrix (ECM) with active erosion sites [27]. Following on from this preclinical study, here we investigate human bone biopsies of MGUS, SMM and newly diagnosed MM patients with high resolution microCT for ultra-structural characterization of osteocyte lacunar morphology, to identify alterations that can be linked to osteolysis and disease progression.

2. Materials and methods

2.1. Patient sample collection and clinical evaluation

The purpose of this study was to determine whether changes in osteocyte lacunae volume and shape distribution could be detected in mineralized bone biopsy samples from patients with MGUS, SMM and newly diagnosed MM. Patients with MGUS ($n = 3$), SMM ($n = 2$) and symptomatic MM ($n = 6$) were diagnosed following the revised international staging system [22]. Clinical data from eleven patients including reports of the low-dose CT scans are given in Tables 1–3. Values in brackets show the normal range for the parameters. The investigators who performed the bench studies were blind to the patient information. This study was approved by the Ethics Committee of the University of Würzburg, Germany (76/13 and 82/20-am). Included patients had an informed consent for the bone biopsy, with a known history of MGUS, SMM, symptomatic MM, lymphoma, leukemia, myelodysplastic syndrome, or myeloproliferative disorders. Patients receiving a bone biopsy based on other diseases like a bone marrow carcinosis were excluded from the study. As control bone biopsy samples, two different data sets were used (Table 4). One Jamshidi bone biopsy sample (2 mm diameter) was obtained from a patient of the University Hospital Würzburg with myelodysplastic syndrome and no diagnosis of MGUS, SMM or MM. Three cylindrical transiliac samples (5 mm diameter) were obtained from an earlier study [8] on autopsy samples at the Ludwig Boltzmann-Institute of Osteology Vienna. Osteocyte lacunae characteristics were re-evaluated in the current study. For all control and disease bone biopsy samples, the trabecular bone compartment was analyzed and the cortical bone was excluded. Trabecular bone is the first contact region with MM cells and comprises the larger fraction of bone in Jamshidi biopsies. Cortical bone was not present in some biopsies, as we received left over tissue from diagnostic procedures. Only biopsy samples containing sufficient amount of trabecular bone, which maintained sample integrity without loss of bone structure (bone debris) caused by the extraction procedure, were considered.

The patient clinical data (Tables 1–3) include: biopsy number, disease stage (MGUS, SMM or newly diagnosed MM), age, gender, immunoglobulin subtypes (heavy and light chains) secreted by malignant plasma cells, revised International Staging System (r-ISS), cytogenetic risk, M-protein secreted by plasma cells at time of diagnosis (g/L), heavy chain (mg/dL), involved serum free light chain (sFLC) (mg/L), ratio (involved/uninvolved sFLC), bone marrow infiltration (%) based on immunohistochemistry Syndecan-1 (CD138) with >60 % corresponding to newly diagnosed MM, computed tomography findings of osteolytic lesions, hemoglobin (g/dL), creatinine (mg/dL) and cytogenetic alterations by fluorescence in situ hybridization (FISH), which allows for detection of genetic changes which are relevant for the ISS stage. In

Table 1
Clinical data from MGUS patients.

Parameters	MGUS 1	MGUS 2	MGUS 3
Biopsy number	MGUS 1	MGUS 2	MGUS 3
Age (years)	71	60	68
Gender	f	m	f
Immunoglobulin subtype	IgG lambda	IgG kappa	IgG kappa
r-ISS	not applicable	not applicable	not applicable
Cytogenetic risk	not applicable	not applicable	not applicable
M-protein [g/L]	not detectable	not detectable	1.2
Heavy chain [mg/dL, normal range]	1382 (610–1616) ^a	881 (610–1616)	507 (610–1616)
Involved serum free light chain (sFLC) [mg/L, normal range]	23.89 (5.71–26.30)	10.75 (3.30–19.40)	215 (3.30–19.40)
Ratio (involved / uninvolved sFLC)	0.86	1.02	5.44
Bone marrow infiltration of CD138 ⁺ cells [%]	<10	<10	<5
CT findings of osteolytic lesion	none	none	none
Hemoglobin [g/dL]	12.9 (12–16)	14.4 (13.5–16.9)	12.7 (12–16)
Creatinine [mg/dL]	0.63 (0–0.95)	1.06 (0–1.17)	6.69 (0–0.95)
Cytogenetics ^b	no aberration	no aberration	no aberration
Calcium [mmol/L]	2.2 (2.0–2.7)	2.5 (2.0–2.7)	2.3 (2.0–2.7)
Alkaline phosphatase [U/L]	51 (35–105)	72 (35–105)	not available
Inorganic phosphate [mmol/L]	1.09 (0.87–1.45)	1 (0.87–1.45)	1.85 (0.87–1.45)
Bone anti-resorption treatment (duration)	Denosumab (four months)	no	no

^a Values in brackets show the normal range for the parameters, respectively.

^b Cytogenetic alterations by fluorescence in situ hybridization (FISH).

Table 2
Clinical data from SMM patients.

Parameters	SMM 1	SMM 2
Biopsy number	SMM 1	SMM 2
Age (years)	46	70
Gender	f	m
Immunoglobulin subtype	IgA kappa	IgA lambda
r-ISS	II	I
Cytogenetic risk	high risk	standard risk
M-protein [g/L]	not detectable	13.42
Heavy chain [mg/dL, normal range]	1826 (88–410)	2826 (88–410)
Involved serum free light chain (sFLC) [mg/L, normal range]	11.82 (3.30–19.40)	54.99 (5.71–26.3)
Ratio (involved / uninvolved sFLC)	1.33	12.03
Bone marrow infiltration of CD138 ⁺ cells [%]	10–15	20–30
CT findings of osteolytic lesion	none	none
Hemoglobin [g/dL]	12 (12–16)	13.2 (13.5–16.9)
Creatinine [mg/dL]	0.78 (0–0.95)	0.91 (0–1.17)
Cytogenetics	t4;14, gain of 1q21	del13q14
Calcium [mmol/L]	2.2 (2.0–2.7)	2.4 (2.0–2.7)
Alkaline phosphatase [U/L]	59 (35–105)	40 (35–105)
Inorganic phosphate [mmol/L]	1.08 (0.87–1.45)	1.23 (0.87–1.45)
Bone anti-resorption treatment (duration)	not known	no

addition, parameters describing the bone metabolism include: calcium (mmol/L), alkaline phosphatase (U/L), phosphate (mmol/L) and finally, bone anti-resorption treatment ongoing at the time of biopsy.

2.2. Immunohistochemical detection of CD138 on decalcified bone paraffin sections

Paraffin embedded human specimens were retrospectively collected from formalin-fixed paraffin-embedded tissue of anonymized samples, archived at the Institute of Pathology, University of Würzburg. Shortly, Jamshidi bone biopsy samples that were derived from the clinical department of the University of Würzburg were fixed for 24 h in formalin, decalcified for 24 h at 37 °C using an EDTA-based approach, dehydrated with alcohol and xylene and then embedded in paraffin.

For the immunohistochemical detection of CD138/Syndecan-1 expression, sections were deparaffinized. The tissue was hybridized with an antibody against CD138/Syndecan-1 (clone MI15, mouse, #M7228, Agilent, Santa Clara, CA, USA), following standard procedures by automated processing using the Tecan Evo Freedom stainer and the Dako Advance system according to the manufacturer's protocol.

2.3. Microcomputed tomography (microCT): image acquisition

Specimens were scanned using an EasyTom micro/nano tomograph (RX solutions, France). Low resolution scanning parameters were: 107 kV, 93 µA, 7 µm voxel size, frame rate of 3, average frame of 5. High resolution scanning parameters were: 60 kV, 124 µA, 1–2 µm voxel size, frame rate of 1, average frame of 5. Reconstruction of the 1120 projections/scan were performed using RX Solutions X-Act software.

2.4. Low resolution microCT: image analysis

The overall bone biopsy morphology with particular focus on trabecular bone thickness was analyzed with Dragonfly software, Version 2022.1 for [Windows], Comet Technologies Canada Inc., Montreal, Canada; software available at <https://www.theobjects.com/dragonfly>. Low resolution microCT stack images (voxel size of 7 µm) were segmented using Otsu thresholding (noise removal of these microCT images and objects was not necessary). A mesh was then created from each individual region of interest (ROI) of the trabecular bone.

The trabecular bone strut thickness was automatically generated and measured from each mesh by Dragonfly software. For this, we calculated

Table 3
Clinical data from newly diagnosed MM patients.

Parameters			
Biopsy number	MM 1	MM 2	MM 3
Age (years)	58	57	72
Gender	m	m	f
Immunoglobulin subtype	IgG kappa	kappa	IgG lambda
r-ISS	III	II	III
Cytogenetic risk	high risk	standard risk	high risk
M-protein [g/L]	35.3	not detectable	20.6
Heavy chain [mg/dL, normal range]	4765 (610–1616)	not available	3074 (610–1616)
Involved serum free light chain (sFLC) [mg/L, normal range]	71.12 (3.30–19.40)	8260 (3.30–19.40)	1376 (5.71–26.3)
Ratio (involved / uninvolved sFLC)	40.41	890.09	355.56
Bone marrow infiltration of CD138 ⁺ cells [%]	70	60–70	90
CT findings of osteolytic lesion	osteolytic lesion with extraosseous soft tissue mass in spine (T12), lytic lesion in pelvis, rib series fractures, medullary lesions in femora and humeri, reduced bone mineral density	disseminated osteolysis in spine, one large lesion in T9 with increased fracture risk, old vertebral body collapse in T7 and fracture of the fourth left rib, multiple small osteolyses in scapulae, ribs, sternum reduced bone mineral density	no osteolytic lesions medullary lesions in upper and lower limbs, spine, sternum; reduced bone mineral density
Hemoglobin [g/dL]	10.8 (13.5–16.9)	10.7 (13.5–16.9)	10.2 (12–16)
Creatinine [mg/dL]	0.83 (0–1.17)	2.3 (0–1.17)	0.72 (0–0.95)
Cytogenetics	t14;16, gain of 1q21	t11;14	del 17p, 1q gain, del14q, del 4p, del 16q, del 5p
Calcium [mmol/L]	2.3 (2.0–2.7)	2.9 (2.0–2.7)	2.5 (2.0–2.7)
Alkaline phosphatase [U/L]	97 (35–105)	80 (35–105)	49 (35–105)
Inorganic phosphate [mmol/L]	1.25 (0.87–1.45)	1.33 (0.87–1.45)	0.99 (0.87–1.45)
Bone anti-resorption treatment (duration)	bisphosphonate (zoledronic acid) for one month	no	no

Parameters			
Biopsy number	MM 4	MM 5	MM 6
Age (years)	60	68	64
Gender	m	f	f
Immunoglobulin subtype	IgA lambda	IgG kappa	IgG kappa
r-ISS	II	II	II
Cytogenetic risk	standard risk	standard risk	standard risk
M-protein [g/L]	32.6	4.5	7.4
Heavy chain (mg/dL, normal range)	4000 (88–410)	1180 (610–1616)	1625 (610–1616)
Involved serum free light chain (sFLC) [mg/L, normal range]	33.8 (5.71–26.3)	16.59 (3.30–19.40)	309.8 (3.30–19.40)
Ratio (involved / uninvolved sFLC)	4.26	1.49	8.41
Bone marrow infiltration of CD138 ⁺ cells [%]	30	50	60
CT findings of osteolytic lesion	osteolytic lesion in pelvis; mild reduction in bone mineral density	disseminated osteolysis in skull, spine, fracture series in spine (T7, 8, 11; L1, 2, 4), reduced bone mineral density in spine	none
Hemoglobin [g/dL]	14 (13.5–16.9)	10.1 (12–16)	12.8 (12–16)
Creatinine [mg/dL]	0.96 (0–1.17)	1.02 (0–0.95)	0.91 (0–0.95)
Cytogenetics	del 1p32, del13q14, gain of 1q21	trisomy 11	gain of 1q21
Calcium [mmol/L]	2.4 (2.0–2.7)	2.5 (2.0–2.7)	2.4 (2.0–2.7)
Alkaline phosphatase [U/L]	41 (35–105)	95 (35–105)	92 (35–105)
Inorganic phosphate [mmol/L]	1.19 (0.87–1.45)	0.94 (0.87–1.45)	0.74 (0.87–1.45)
Bone anti-resorption treatment (duration)	no	no	no

the median, first and third quartile, minimum and maximum values of about 3–5.5 10⁶ local vertices created between boundary points of each overall mesh. The software calculated these vertices as diameters of hypothetical spheres that fit within each boundary point of the mesh. The trabecular bone strut thickness distribution is depicted with a colour code for each biopsy and as a box plot.

2.5. High resolution microCT: image analysis

The volume of interest (VOI) within the high resolution scans were selected in such a way so that the bone volume to be analyzed was maximized. The empty cavities within mineralized tissue corresponding to osteocyte lacunae were segmented. Based on previous studies with

Table 4
Control samples: Jamshidi bone biopsy and samples from autopsies.

Parameters				
Biopsy number	control 1	control 2	control 3	control 4
Type of biopsy	jamshidi	autopsy ^a	autopsy ^a	autopsy ^a
Age (years)	69	64	57	63
Gender	f	f	f	f
Previous disease	myelodysplastic syndrome	not known	not known	not known

^a Subset of an earlier cohort presented previously [8] and re-evaluated here.

healthy trabecular bone [8,28–30], cavities smaller than 20 μm³ and larger than 3000 μm³ were considered cracks or artifacts and excluded from the analysis.

2.5.1. Segmentation of osteocyte lacunae

The stack of high resolution microCT images (1–2 μm voxel size) was segmented using Otsu thresholding in Dragonfly. For these images, noise removal was performed using 3D smoothing (kernel of 3) as morphological operation. Next, the binary mask was used to extract the pores. Osteocyte lacunae were filled in a copy of the binary mask using a filling morphological operation. Next, the multi-ROI conversion tool of Dragonfly was used to select each lacuna individually. This tool allowed to define each osteocyte lacuna as an individual ROI, hence enabling the calculation of each lacunae volume and shape. The generated binary images were then used for the quantitative analysis of lacunae volume and shape with Python software (version 3.5). The script used was written in a Jupyter notebook with Python software (version 3.7). External libraries not contained in the Anaconda environment were installed from their repository. Micropores smaller than 20 μm³ and larger than 3000 μm³ were considered cracks or artifacts and excluded from the analysis. For the purpose of this study, two separate lacunar volume ranges were investigated: small lacunae 20–900 μm³ (osteocyte lacunar microporosity characteristic of healthy bone [28,31]), and larger lacunae 900–3000 μm³ (microporosity potentially associated to bone disease).

2.5.2. Osteocyte lacunar volume analysis

For the osteocyte lacunar volume analysis, each segmented lacunar volume was calculated as the total number of voxels times the volume of a single voxel. Based on this, we could define the number of lacunae (Lc. N) of a given lacunar volume (Lc.V). We could also define the total

Table 5
Nomenclature for osteocyte lacunar volume analysis.

Nomenclature	Abbreviation	Unit
Number of osteocyte lacunae	Lc.N	–
Total number osteocyte lacunae	Lc.TN	–
Lacunar volume	Lc.V	μm ³
Total lacunar volume	Lc.TV	μm ³
Trabecular bone total volume	Tb.TV	μm ³

Table 6
Nomenclature for osteocyte lacunar analysis.

Parameter	Definition	Unit	Formula
Normalized lacunar volume frequency distribution	Number of lacunae volume divided by the trabecular bone total volume minus the lacuna total volume	#/μm ³	$\frac{\sum Lc.N}{Tb.TV - Lc.TV}$
Lacunar volume cumulative distribution	Sorted sum of volume divided by total volume	–	–
Microporosity	Total lacunar volume with respect to the trabecular bone total volume	–	$\frac{Lc.TV}{Tb.TV}$
Lacuna elongation	0 for elongated 1 for spherical	–	$\frac{EV1}{EV2}$
Lacuna flatness	0 for flat 1 for spherical	–	$\frac{EV1}{EV3}$
Lacuna anisotropy	0 for isotropic, spherical 1 for highly anisotropic	–	$1 - \frac{EV2}{EV1}$

number of osteocyte lacunae (Lc.TN), total lacunar volume (Lc.TV) and trabecular bone total volume (Tb.TV). This nomenclature and units are summarized in Table 5.

2.5.3. Normalized lacunar volume frequency distribution and lacunar density

To plot the lacunar volume frequency distribution, all lacunae within one sample were stratified according to lacunar volume intervals. For a discrete lacunar volume interval of 20 μm³, we quantified the number of osteocyte lacunae (Lc.N.) for that given size. For a given lacunar volume (Lc.V), we quantified the lacunar number (Lc.N), normalized to the trabecular bone total volume (Tb.TV) and excluding the total lacunar volume (Tb.TV-Lc.TV), to account for size differences between samples, since larger samples have more lacunae than smaller ones, as well as for potential differences in the trabecular bone microporosity. The data is presented as the frequency in a histogram with a bin size of 20 μm³. Furthermore, the lacunar density was calculated as the total number of osteocyte lacunae (Lc.TN) normalized to the trabecular bone total volume and excluding lacunar total volume (Tb.TV-Lc.TV), in other words, the summation of the osteocyte lacunar volume frequency distribution. This was done for both ranges separately, small lacunae 20–900 μm³ and larger lacunae 900–3000 μm³.

2.5.4. Lacunar volume cumulative distribution

The cumulative distribution is calculated by sorting all osteocyte lacunae by volume, from smallest to largest, and increasing the count of the fraction 1/N at each point, with N = length of array. The cumulative lacunae volume distribution was plotted with respect to the lacunae volume (Lc.V), with the x axis showing a given lacunae volume and the y axis showing the cumulative volume. The 50 % cutoff illustrating the specific volume below which half of all osteocyte lacunae are contained, was marked with a dashed line.

2.5.5. Osteocyte lacunar microporosity analysis

The microporosity was calculated as the lacunar total volume (Lc. TV) divided by trabecular bone total volume (Tb.TV) for each group. This was done for both ranges separately, small lacunae 20–900 μm³ and larger lacunae 900–3000 μm³.

2.5.6. Osteocyte lacunar morphological analysis

To perform the lacunar morphological analysis, the resulting shape of a lacuna and model representation consists of a 3 × 3 matrix of the positions of the voxels in a lacuna. For a diagonal symmetric matrix defining an ellipsoid, this is converted into the eigenvectors of the matrix, which correspond to the major and minor axes of the ellipsoid. From the eigenvectors, the corresponding eigenvalues (EV) were derived (EV1 > EV2 > EV3), where EV1 is the largest eigenvalue and EV3 the smallest [32,33]. Three parameters were assessed to examine lacunae morphology, based on the eigenvalues of each individual lacuna: the lacuna elongation, flatness and anisotropy [34]. This nomenclature and units are summarized in Table 6. In short, lacuna elongation (EV2/EV1, ratio of medium to largest eigenvalue) ranged from lower

values for elongated and 1 for spherical; lacuna flatness (EV3/EV2, ratio of smallest to medium eigenvalue) ranged from 0 for flat to 1 for spherical; and lacuna anisotropy (1-EV3/EV1, one minus the ratio of smallest to largest eigenvalue) ranged from 0 for isotropic/spherical to 1 for highest anisotropy.

2.6. Statistical analysis

A total of $n = 15$ bone biopsy samples were analyzed, including MGUS $n = 3$, SMM $n = 2$, newly diagnosed MM $n = 6$ and control biopsy samples $n = 4$ (Jamshidi $n = 1$ and from autopsies $n = 3$). Additional

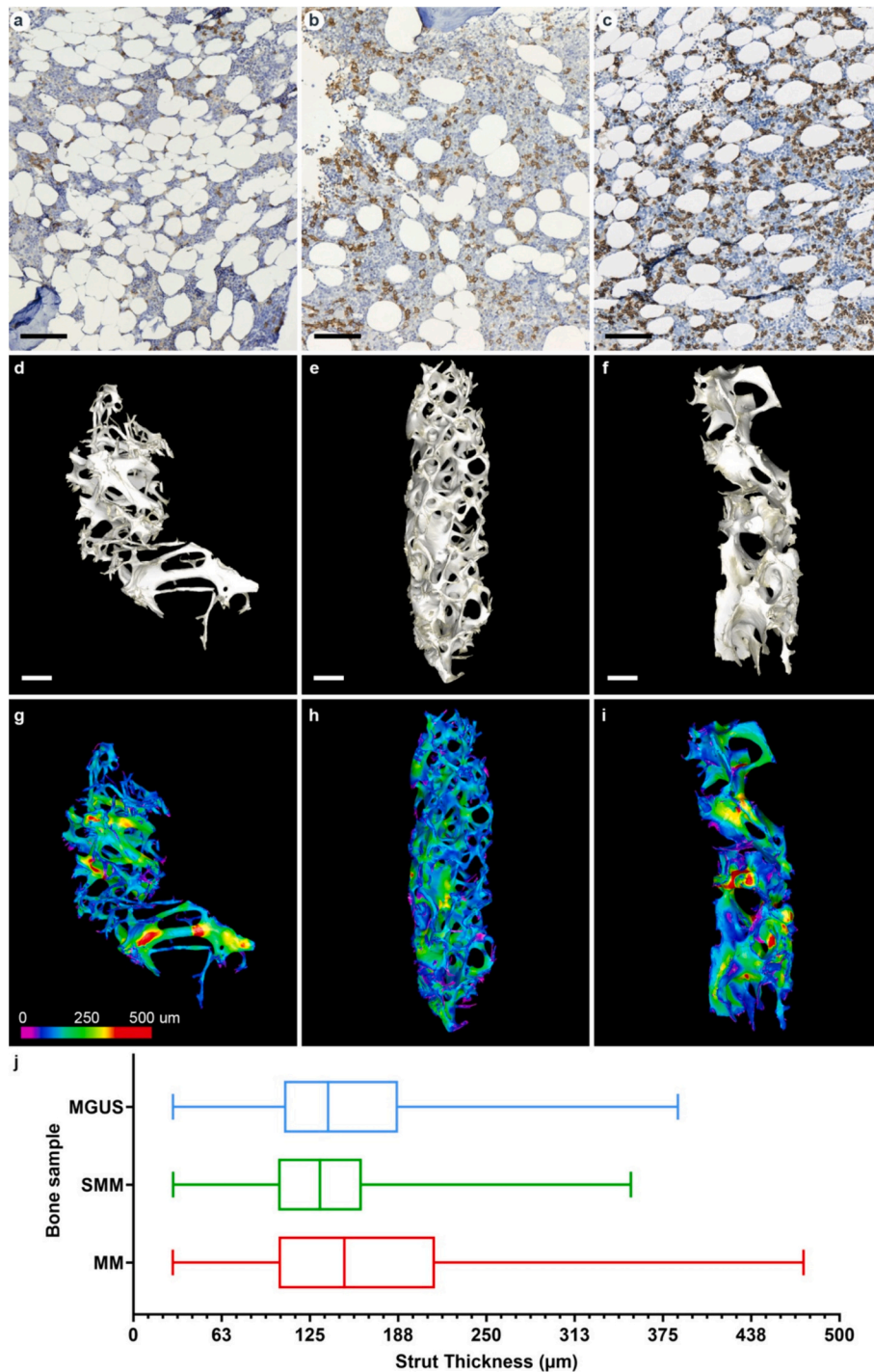


Fig. 1. Immunohistochemical (IHC) CD138 staining and low resolution microCT overview of the bone biopsies from patients with: (a, d, g) monoclonal gammopathy of undetermined significance (MGUS), (b, e, h) smoldering myeloma (SMM), and (c, f, i) newly diagnosed multiple myeloma (MM). (a-c) Representative light microscopy images of the bone marrow compartment from the biopsy samples: CD138 positive staining in brown, cell nuclei counterstain in blue. MGUS bone biopsy #MGUS 2 with <10 % bone marrow infiltration, SMM bone biopsy #SMM 1 with 10–15 % bone marrow infiltration, MM bone biopsy #MM 1 with 70 % bone marrow infiltration. (d-f) 3D reconstructions of low resolution (7 μm voxel) microCT scans of representative bone biopsies. (g-i) Quantitative analysis of trabecular bone strut thickness distribution and colour code visualization with Dragonfly software. (j) Distribution of trabecular thickness shown with median, first and third quartile. Scale bars equal to 100 μm (a-c), 1 mm (d-f). (For interpretation of the references to colour in this figure legend, the reader is referred to the web version of this article.)

bone biopsy samples ($n > 15$) were collected but excluded from the analysis due to lack of sample integrity (e.g. loss of bone structure (bone debris) during the extraction procedure) or insufficient amount of trabecular bone. To analyze the differences in bone microporosity and lacunar morphological analysis, a one-way analysis of variance (ANOVA) with Tukey's multiple comparisons test ($*p < 0.05$) was used (GraphPad Prism 8.0 software).

3. Results

3.1. Clinical data and patient history

Clinical data from patients of the University Hospital Würzburg and parameters describing bone metabolism are compiled in [Tables 1–3](#). The cohort included patient-derived bone biopsy samples with the precursor condition MGUS ([Table 1](#)), SMM ([Table 2](#)), and newly diagnosed MM ([Table 3](#)). MGUS is diagnosed when monoclonal immunoglobulins (< 3 g/dL) are detected in the serum of patients and < 10 % abnormal plasma cells are found in the bone marrow. When MGUS continuously progresses, the condition is named SMM, when between 10 and 60 % plasma cells are detected and monoclonal immunoglobulin levels are higher than 3 g/dL. SMM differs from symptomatic MM, a stage in which CRAB symptoms of hypercalcemia, renal insufficiency, anemia and

osteolytic bone lesions occur [[35](#)]. The revised International Staging System for Multiple myeloma (r-ISS) was used to stratify patients with respect to the relative risk to their survival ([Tables 1–3](#)) [[36](#)]. Control samples obtained from the University Hospital Würzburg and from the Ludwig Boltzmann-Institute of Osteology Vienna are compiled in [Table 4](#).

Patients with MGUS showed no detectable osteolytic bone lesions by low-dose CT scans ([Table 1](#)). One patient with MGUS received denosumab for four months (#MGUS 1, [Table 1](#)). In this case, we cannot exclude that the anti-resorptive treatment interfered with the bone ultrastructure. Similarly, the two patients classified as SMM exhibited no signs of osteolytic lesions by low-dose CT scans at the time of biopsy ([Table 2](#)). Disease staging for SMM was determined based on the percent of bone marrow infiltration of CD138⁺ plasma cells, above 10 %. Patients classified as MM had a bone marrow infiltration of CD138⁺ plasma cells between 60 and 90 % (4 out of 6), a ratio of the involved to the uninvolved free light chain in the serum (sFLC) of >100 (2 out of 6), and/or local or disseminated lytic lesions, as well as reduced bone mineral density (4 out of 6 patients) based on CT findings ([Table 3](#)). All bone turnover markers (phosphate, calcium, alkaline phosphatase) were within normal ranges ([Tables 1–3](#)). Anti-resorptive therapy with the bisphosphonate zoledronic acid had been administered to one MM patient for one month before the biopsy was taken (#MM 1, [Table 3](#)). We

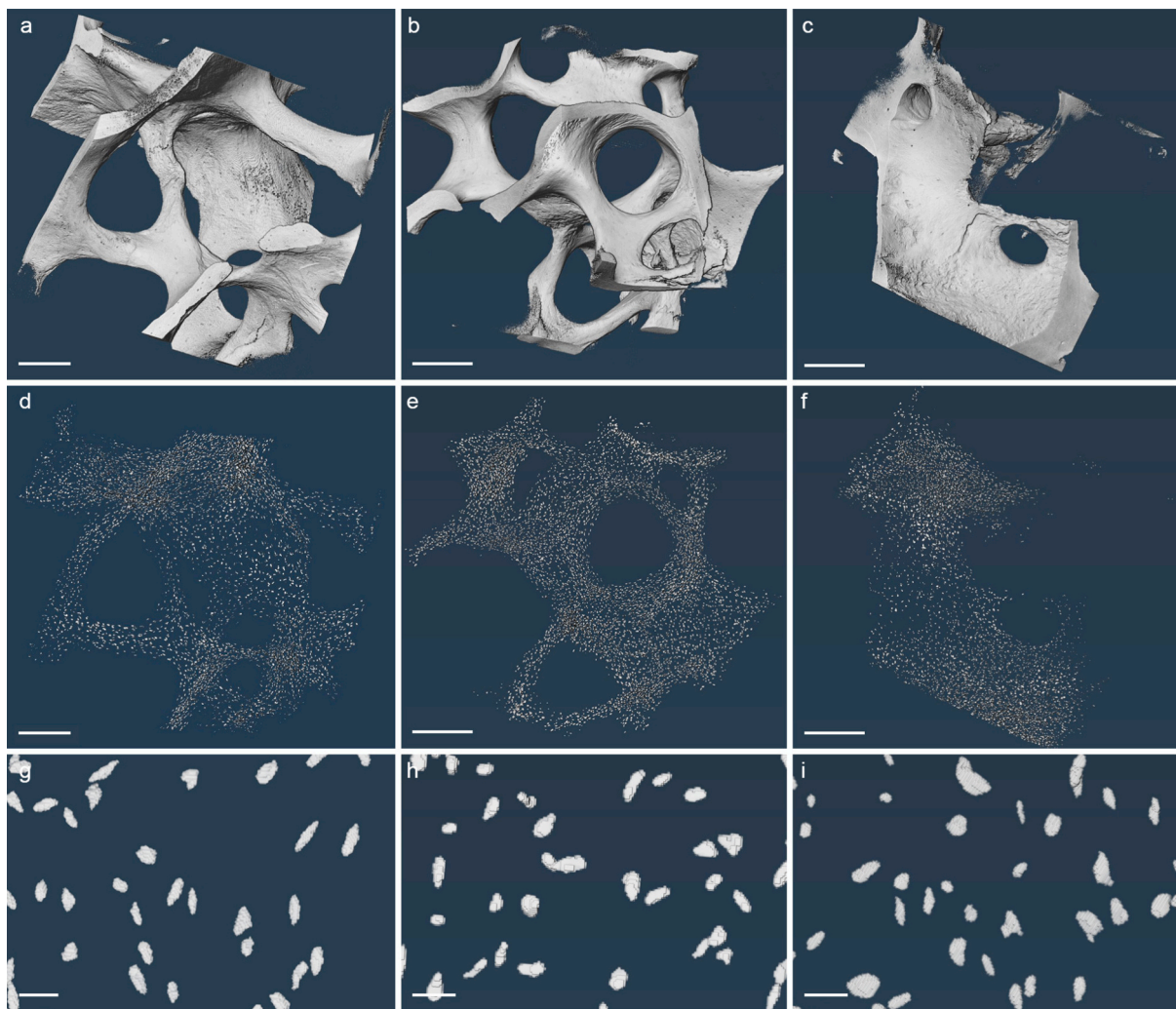


Fig. 2. Bone biopsy macroscopic structure and osteocyte lacunar microporosity visualized with high resolution microCT in MGUS, SMM and MM samples. (a-c) 3D reconstructions of local scans (high resolution microCT; voxel size 1–2 μm) and (d-i) the corresponding segmented osteocyte lacunar microporosity of representative samples: (a, d, g) MGUS bone biopsy #MGUS 2, (b, e, h) SMM bone biopsy #SMM 1, (c, f, i) MM bone biopsy #MM 1. Scale bars equal to 250 μm (a, d), 350 μm (b, e), 400 μm (c, f) and 20 μm (g-i).

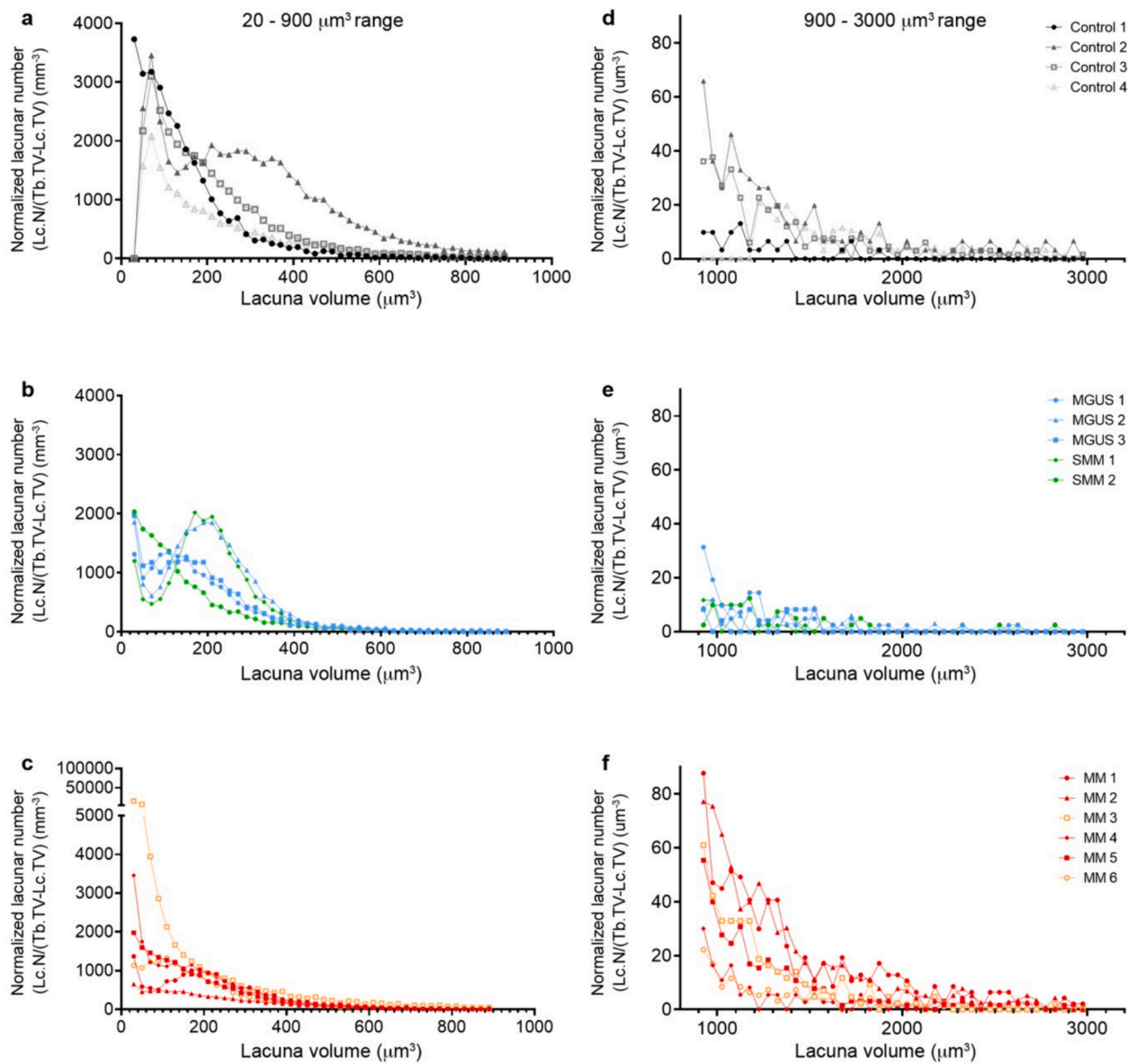


Fig. 3. Lacunar volume frequency distribution of osteocytes in control, MGUS, SMM and MM samples. Frequency distribution normalized to trabecular bone total volume for two separate lacunar volume ranges: 20–900 μm^3 and 900–3000 μm^3 . For each lacunae volume interval (x-axis), number of osteocyte lacunae (Lc.N) normalized by the trabecular bone total volume excluding lacunar total volume (Tb.TV-Lc-TV) (y-axis). Frequency distribution for each group: (a, d) control, (b, e) MGUS and SMM, (c, f) MM. Sample from the Jamshidi biopsy in black, all other control samples in grey. MGUS in blue, SMM in green, MM samples with bone lytic lesion in red, MM samples without lytic lesions in orange. Please note the different scale in the y-axis of subplot c. (For interpretation of the references to colour in this figure legend, the reader is referred to the web version of this article.)

assume that the single dose of the bisphosphonate did not affect bone ultrastructure in such short timeframe.

3.2. Immunohistochemical (IHC) and microcomputed tomography (microCT) overview analysis

As part of the standard clinical practice, and to detect the clonal bone marrow plasma cells and quantify the percent of bone marrow infiltration of CD138⁺ cells, bone biopsies were processed for immunohistochemical (IHC) analysis for CD138 staining. Fig. 1a-c shows representative samples of MGUS, SMM and newly diagnosed MM patients with <10 % for MGUS and >10 % for SMM and MM patients. Biopsies collected from patients were selected after applying exclusion criteria (see Section 2.6 for details). 3D reconstructions of representative images are shown in Fig. 1d-f. Quantification of trabecular thickness

distribution is shown in Fig. 1g-j and Supplementary Fig. S1. No clear differences between MGUS, SMM and newly diagnosed MM were observed in the macroscopic trabecular bone architecture, which motivated the further analysis of bone ultrastructure with high resolution microCT.

3.3. Bone ultrastructure and segmentation of osteocyte lacunar microporosity

We next investigated the bone ultrastructure with a focus on the osteocyte lacunar microporosity. High resolution microCT scans (voxel size 1–2 μm) were performed on smaller VOI (Supplementary Fig. S2). Fig. 2 illustrates an example of VOI of representative samples and the segmented osteocyte lacunar microporosity for MGUS, SMM and newly diagnosed MM, and Supplementary Fig. S3 for a control sample. This

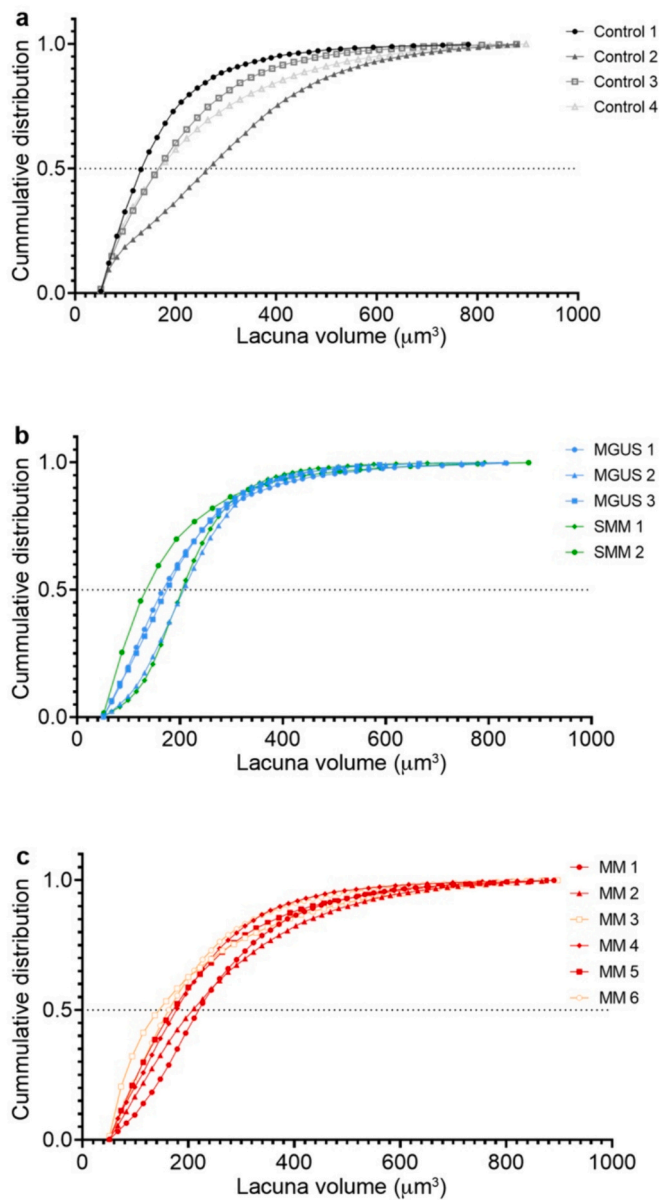


Fig. 4. Lacunar volume cumulative distribution for the small lacunae 20–900 μm^3 range of osteocytes in control, MGUS, SMM and MM samples. Cumulative distribution (from 0 to 1) of lacunae (y-axis) for each volume in μm^3 (x-axis). Cumulative distribution for each group: (a) control, (b) MGUS and SMM, (c) MM. Dashed line indicates the 50 % cutoff volume below which are half of all osteocyte lacunae of one sample. Sample from the Jamshidi biopsy in black, all other control samples in grey. MGUS in blue, SMM in green, MM samples with bone lytic lesion in red, MM samples without lytic lesions in orange. (For interpretation of the references to colour in this figure legend, the reader is referred to the web version of this article.)

segmented osteocyte lacunar microporosity was then quantitatively analyzed for lacunar volume distribution (Figs. 3–4), lacunar density and microporosity (Fig. 5), and lacunar morphological analysis (Fig. 6).

3.4. Analysis of osteocyte lacunar volume distribution and microporosity

First, we characterized the osteocyte lacunar volume distribution, both as a frequency distribution (Fig. 3) and then as a cumulative distribution (Fig. 4). To plot the lacunar volume frequency distribution, all lacunae within one sample were stratified according to volume intervals of 20 μm^3 . Two separate lacunar volume ranges were investigated: small

lacunae 20–900 μm^3 (Fig. 3a-c) (osteocyte lacunar microporosity characteristic of healthy bone [28,31]), and larger lacunae 900–3000 μm^3 (Fig. 3d-f) (microporosity potentially associated to bone disease). Control samples (Fig. 3a, d) were compared with MGUS, SMM (Fig. 3b, e), and newly diagnosed MM (Fig. 3c, f). In the small lacunae range 20–900 μm^3 , we observed a distribution within a comparable range (y-axis from 0 to 4000 μm^3) in the different groups, with the exception of sample #MM 3, which had a much higher number of osteocyte lacunae compared to the other samples within the MM group (Fig. 3c, note the extended y-axis). In contrast, in the larger lacunae range 900–3000 μm^3 , we observe a clearly higher number of lacunae for the MM group (Fig. 3f) compared with MGUS (Fig. 3d) and SMM (Fig. 3e) groups.

When comparing both ranges, we observed a larger number of small osteocyte lacunae (Fig. 3a-c) compared to larger lacunae (Fig. 3d-f). This motivated a more detailed lacunar volume cumulative distribution analysis (Fig. 4), where the lacunar number (Lc.N) was plotted as a cumulative curve. The 50 % cutoff indicates that half of all osteocyte lacunae within one sample are below that specific volume interval (x-axis). In the control group (Fig. 4a), the 50 % cutoff is heterogeneous: samples #control 1, #control 3 and #control 4 have 50 % of the lacunae with volumes around 140–170 μm^3 , while sample #control 2 has the highest volume with 270 μm^3 . In the MGUS/SMM group (Fig. 4b), the 50 % cutoff ranges from 170 to 210 μm^3 , except sample #SMM 2 with the smallest cutoff at 140 μm^3 . In the MM group (Fig. 4c), the 50 % cutoff varies from 150 to 220 μm^3 , with clearly lower values for the biopsies of patients without bone osteolytic lesions (#MM 3 and #MM 6). In conclusion, we observe a trend for increasing 50 % cutoff for more advanced disease, indicating that the sum volume of the smallest 50 % lacunae account for a larger volume as the disease progresses (Fig. 4c). In other words, we observe a shift towards larger lacunae with disease progression.

Next, we calculated the lacunar density as the total number of osteocyte lacunae (Lc.TN) normalized to the trabecular bone total volume and excluding lacunar total volume (Tb.TV-Lc.TV), in other words, the sum of the osteocyte lacunar volume frequency distribution (Fig. 3). This was done for both ranges separately, small lacunae 20–900 μm^3 (Fig. 5a) and larger lacunae 900–3000 μm^3 (Fig. 5b). In the small lacunae range, the mean for the control samples was 29,809 \pm 11,314 lacunae/ mm^3 , for MGUS/SMM 18165 \pm 3278 lacunae/ mm^3 and for MM 20502 \pm 13,827 lacunae/ mm^3 . No significant differences were observed in the small lacunae range, although there was a clear trend for lower lacunar density for diseased samples (MGUS/SMM and MM) compared to the controls. However, in the larger lacunae range 900–3000 μm^3 (Fig. 5b), significantly higher lacunar density was found in the newly diagnosed MM group compared to the MGUS/SMM group.

In order to evaluate the microporosity in relation to the total bone volume, we divided the lacunar total volume (Lc.TV) by trabecular bone total volume (Tb.TV) for each group. This was done for both ranges separately, small lacunae 20–900 μm^3 (Fig. 5c) and larger lacunae 900–3000 μm^3 (Fig. 5d). No significant differences were observed in the small lacunae range. However, in the larger lacunae range, significantly higher microporosity was found in the newly diagnosed MM group compared to the MGUS/SMM group. This is consistent with the observations of lacunar volume frequency distribution (Fig. 3f) and lacunar density (Fig. 5b).

3.5. Analysis of osteocyte lacunar morphology

Next, we aimed to assess whether disease progression could be associated with lacunar morphological changes. To do so, we performed a lacunar morphological analysis in the small lacunae 20–900 μm^3 range in all groups (control, MGUS/SMM and newly diagnosed MM). Based on previous analogous analysis [34], we investigated the distribution of lacunar flatness, elongation and anisotropy. Towards that end, the principal eigenvalues for each osteocyte lacunae were obtained: EV1, EV2 and EV3. The morphological parameters were calculated as

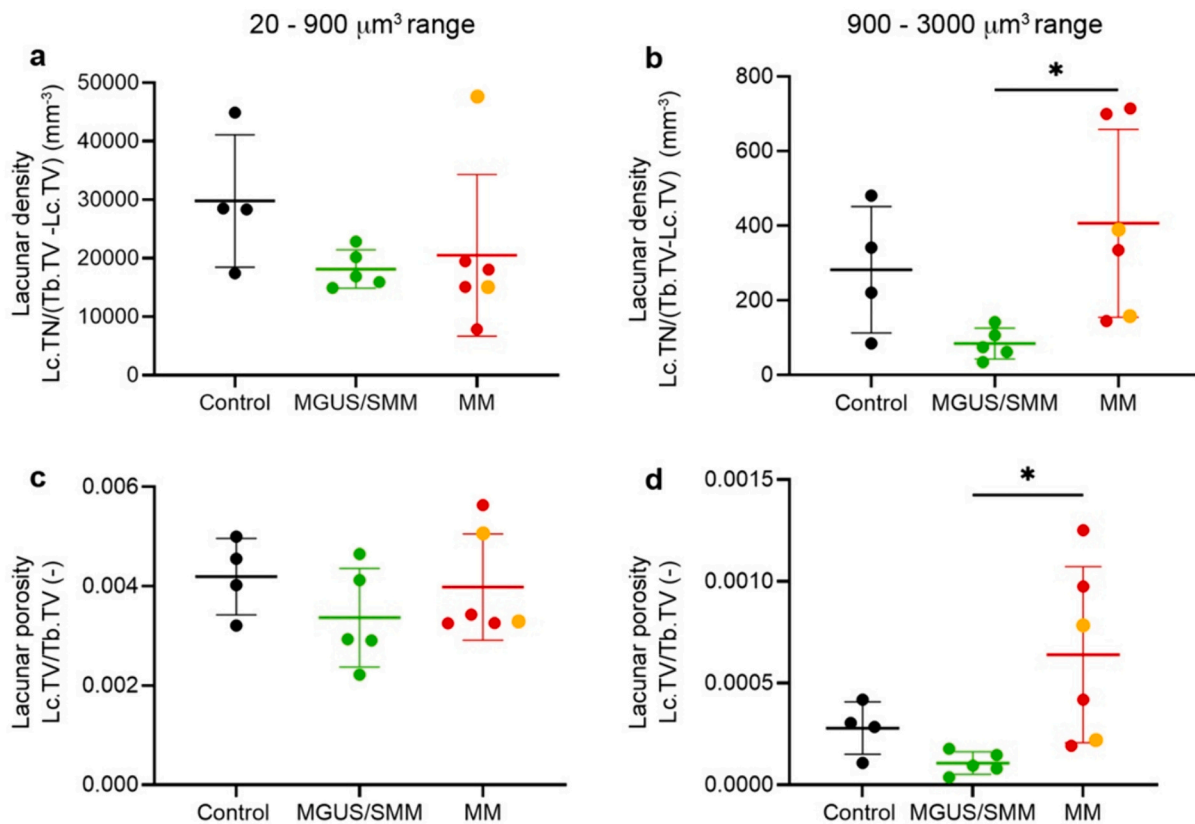


Fig. 5. Lacunar density and microporosity analysis for the small lacunae 20–900 μm^3 range and for the larger lacunae 900–3000 μm^3 range of osteocytes in control, MGUS, SMM and MM samples. Lacunar density calculated as the total number of osteocyte lacunae (Lc.TN) normalized to the trabecular bone total volume and excluding lacunar total volume (Tb.TV-Lc.TV), for each control group, MGUS/SMM and newly diagnosed MM (samples with bone lytic lesion in red, samples without lytic lesions in orange). Microporosity calculated as lacunar total volume (Lc.TV) divided by trabecular bone total volume (Tb.TV) for each group. Error bars indicate mean \pm SD. One way ANOVA with Tukey's multiple comparison test * $p < 0.05$. (For interpretation of the references to colour in this figure legend, the reader is referred to the web version of this article.)

described in Table 6. The lacuna elongation (EV2/EV1, ratio of medium to largest eigenvalue) is shown in Fig. 6a-d; lacuna flatness (EV3/EV2, ratio of smallest to medium eigenvalue) in Fig. 6e-h; and lacuna anisotropy (1-EV3/EV1, one minus the ratio of smallest to largest eigenvalue) in Fig. 6i-l. The fraction of lacunar number (Lc.N) normalized against lacunae total number (Lc.TN) in each sample is shown for each group: control (Fig. 6a, e, i), MGUS/SMM (Fig. 6b, f, j) and MM (Fig. 6c, g, k). The median of all lacuna elongation values for each sample are shown in Fig. 6d; similarly, for flatness in Fig. 6h and anisotropy in Fig. 6l.

Lacuna flatness in MGUS/SMM and newly diagnosed MM groups exhibit a broader spread of the distribution compared to the control group, with a shift towards lower values (flatter shapes). Regarding lacuna elongation and anisotropy, the spread of the distribution for the three groups is comparable. A trend for lower values for lacuna elongation (more elongated) and higher values for lacuna anisotropy (more anisotropic) is observed in the MGUS/SMM group compared to the control group, as shown by the curves and the by the median values. However, the differences of the median values are not significant.

4. Discussion

Changes in the volume and shape of osteocytes were identified in previous studies of bone metastasis from breast and prostate cancer and were indicators of osteolysis [13–16]. However, high resolution microCT characterization of osteocyte lacunae in human bone biopsies of MGUS, SMM and newly diagnosed MM has not yet been performed, nor have changes in morphology of osteocytes been linked to patterns of

osteolysis and disease progression. In this context, quantitative analyses of microCT demonstrate altered lacunae volume and shape distribution between MGUS, SMM and newly diagnosed MM. Specifically, we found a significantly higher number of larger lacunae in the 900–3000 μm^3 range, in the MM group compared to the MGUS/SMM group, as reflected in higher lacunar volume frequency distribution (Fig. 3f) and significantly higher lacunar density (Fig. 5b). Consistent with the observation of an increase in lacunar volume frequency distribution, we also found significantly higher microporosity for the larger lacunae range in the MM group compared to the MGUS/SMM group (Fig. 5d).

In the small lacunae 20–900 μm^3 range, the lacunar density for control samples with 29,809 \pm 11,314 lacunae/ mm^3 (Fig. 5a) is in the range previously reported in the literature for 3D analysis of osteocyte morphometry in healthy transiliac bone biopsies [28], which confirms the validity of our analysis. Interestingly, there was a trend for lower lacunar density for diseased samples (MGUS/SMM and MM) compared to the controls, though the differences were not significant (Fig. 5a). This could be indicative of micropetrosis, i.e. osteocyte lacunae mineralization following osteocyte apoptosis [37,38]. Since a lower lacunar density can distinguish healthy, osteoporotic and bisphosphonate-treated osteoporotic patients, it is currently being considered as a novel bone microstructural marker of impaired bone quality [37]. In addition, we observed a trend for increasing values of the 50 % cutoff in the lacunar volume cumulative distribution for more advanced disease, showing that the sum volume of the smallest 50 % lacunae account for a larger volume as the disease progresses (Fig. 4). In terms of shape distribution, the MGUS/SMM group showed a trend for lower lacuna flatness (flatter), lower lacuna elongation (more

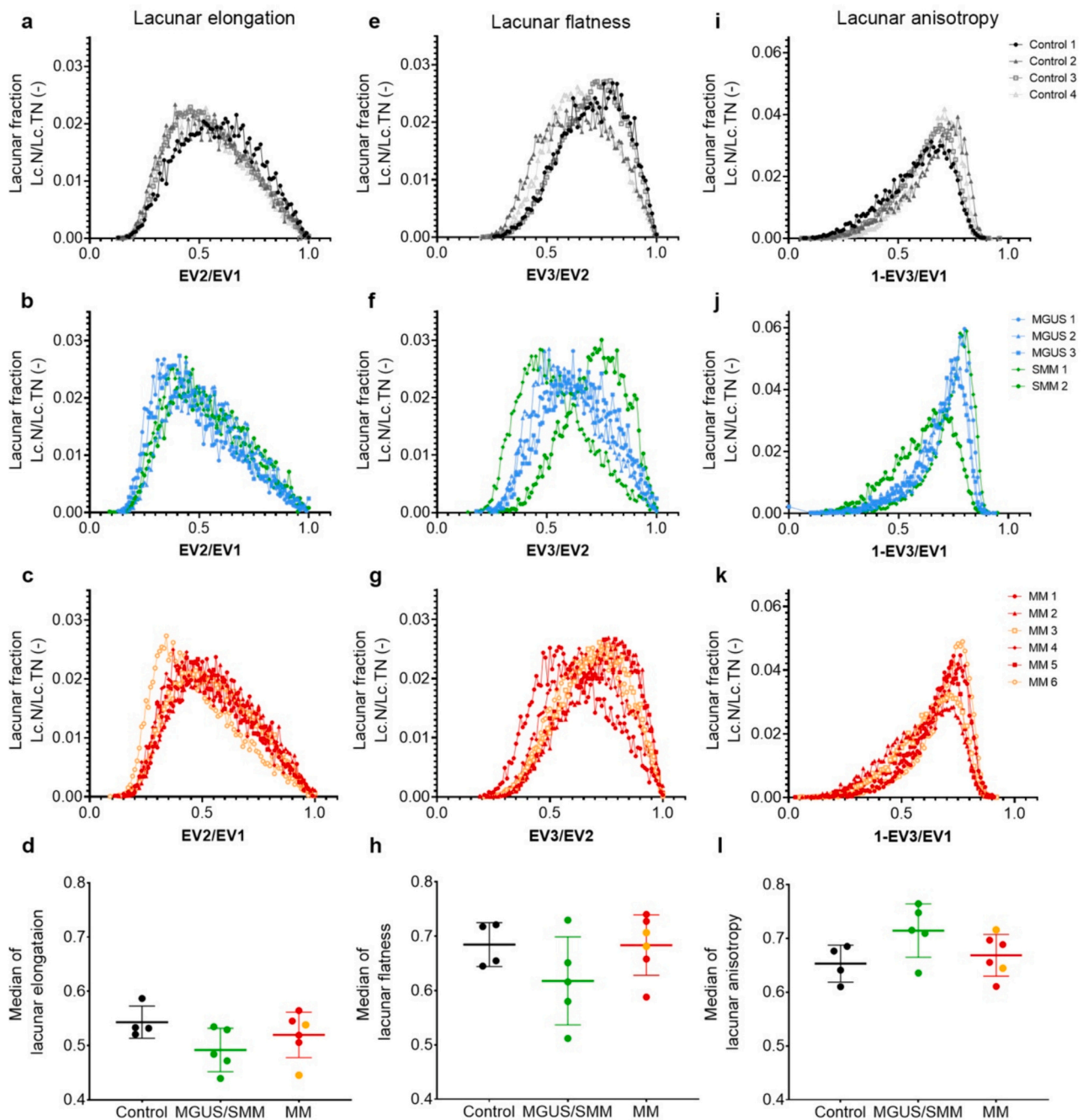


Fig. 6. Lacunar morphological analysis for the small lacunae 20–900 μm^3 range of osteocytes in control, MGUS, SMM and MM samples. Lacunae elongation, flatness and anisotropy analysis for (a, e, i) control, (b, f, j) MGUS/SMM and (c, g, k) MM groups. Individual lacunae were assigned with eigenvalues (EV1, EV2 and EV3) to then calculate lacuna elongation as EV2/EV1 (with lower values for elongated and 1 for spherical) as (a-c) lacunar fraction (Lc.N/Lc.TN) and as (d) median of all lacuna elongation values for each sample; lacuna flatness as EV3/EV2 (ranging from 0 for flat to 1 for spherical) as (e-g) lacunar fraction (Lc.N/Lc.TN) and as (h) median of all lacuna flatness values for each sample; and lacuna anisotropy as 1-EV3/EV1 (with smaller values for isotropic/spherical and 1 for highest anisotropy) as (i-k) lacunar fraction (Lc.N/Lc.TN) and as (l) median of all lacuna anisotropy values for each sample. Sample from the Jamshidi biopsy in black, all other control samples in grey. MGUS in blue, SMM in green, MM samples with bone lytic lesion in red, MM samples without lytic lesions in orange. Error bars indicate mean \pm SD. (For interpretation of the references to colour in this figure legend, the reader is referred to the web version of this article.)

elongated), and higher lacuna anisotropy (more anisotropic) compared to the control group (Fig. 6). Altogether, the findings of a trend for lower lacunar density and a shift towards larger lacunae (increasing 50 % cutoff of the lacunar volume cumulative distribution) for diseased samples (MGUS/SMM and MM) compared to control, in the small lacunae 20–900 μm^3 range; together with significantly higher lacunar density and microporosity for the newly diagnosed MM group, in the larger lacunae 900–3000 μm^3 range, suggest that the osteocytes in MM

bone disease and the precursor conditions MGUS/SMM are undergoing changes in their lacunae morphology during disease progression.

In relation to previous work, currently this is the first study evaluating human bone biopsies at the microstructural level, and so we can only refer to similar work in preclinical setting. Indeed, our established mouse model of MM bone disease was assessed for ultrastructural characterization of the mineralized and nonmineralized ECM, particularly of the osteocyte LCN in early stages of the disease [27,39–41].

Skeletally mature mice were injected with MM cells and the osteocyte LCN architecture was analyzed using advanced imaging techniques, such as high resolution microCT, synchrotron phase contrast-enhanced microCT and confocal laser scanning microscopy (CLSM) [27]. Similar as in human samples, we identified alterations in the osteocyte morphology in the early MM lesions and showed larger, irregular-shaped osteocyte lacunae within a disorganized canaliculi network, compared to flat osteocyte lacunae organized in a lamellar structure in healthy bone [27]. MM affected regions revealed that the lacunae volume was greater and the density was sparser compared to control bones [27]. These data are in concordance with the human MM samples in which a higher number of larger lacunae and a lower lacunar density were detected in the MM group compared to the precursor conditions and control samples. Overall, the MM preclinical model served to predict the changes in the osteocyte lacunae, which in human bone biopsies occurred as a result of progression from MGUS to MM, and thus aligning the preclinical observations with the human findings.

In a recent study in immunocompetent mice, breast and prostate cancer cells were intratibially injected and the changes in the osteocyte LCN induced by tumor cells were analyzed by histology, microCT imaging and CLSM [20]. Interestingly, large lacunae and vascular canals were not observed in the proximity of osteolytic lesions, whereas these changes occurred in osteosclerotic lesions adjacent to prostate cancer cells [20], indicating that changes of osteocyte lacunae characteristics are tumor type-specific. In our study of human biopsy samples with newly diagnosed MM and the precursor conditions, we observed a significantly higher lacunar density in the MM group compared to the MGUS/SMM groups. These observed changes may be related to the presence of osteocytic osteolysis [42], a process that involves osteocytes mobilizing calcium and phosphate, using carbonic anhydrase and vacuolar ATPase to demineralize the bone matrix, and digest protein using matrix metalloproteases and tartrate-resistant acid phosphatase (TRAP) [20,43–45]. In the above-mentioned mouse model [20], TRAP-positive osteocytes in combination with large lacunae were detected in osteosclerotic regions of breast and prostate infiltrated bones, indicating that this mechanism could contribute to the observed increase in lacunae volume [20,43–45]. Whether osteocytic osteolysis plays a role in the progression from healthy to MGUS/SMM to MM bone is not known and warrants further studies. Moreover, since the osteocyte remodeling function affects the lacunae morphology and the LCN architecture, it is likely that changes in the latter are indicators for impaired bone remodeling activity and mechanoresponsiveness.

In order to understand the implications of altered lacunae volume and shape distribution in MM, future studies should consider several factors. First, there is a need for more bone biopsies in i) each of the groups and ii) with sufficient quality to obtain a larger sample size and validate the findings of this study, iii) at other sites of the skeleton where imaging, for example via PET-CT, has shown infiltration of the bone, and iv) from males and females at the ratio of the occurrence of the disease. Second, it is important that the bone biopsies are obtained from comparable anatomical sites to minimize the natural osteocyte volume and shape variation within healthy bone [8,28,46]. Third, although previous studies have used a comparable voxel size of 1.2 μm for lacunar imaging in human bone biopsies [11,28], to further investigate the relationship between osteocyte lacunae and MM, researchers could increase the volume of interest scanned at high resolution (1 μm voxel size or lower) using synchrotron phase-contrast microCT. Fourth, there is a lack of detailed information whether the biopsies were extracted from bone regions affected or unaffected by the disease. Therefore, it remains uncertain whether the evaluated osteocytes accurately reflect the disease stage. For ethical and practical considerations, the bone samples used in the present study were extracted through a standardized approach from the posterior superior iliac crest. Finally, the use of mouse models of MM may provide a valuable tool for investigating the mechanisms underlying the observed alterations in osteocyte lacunae morphology and other aspects of bone ultrastructure, such as LCN architecture, bone

composition, and micro- and nanoscale organization of the organic and inorganic matrix. Furthermore, these models can be used to study how alterations of the osteocyte lacunar morphology affect the response of osteocytes to local tissue strains, their remodeling capacity of mineralized bone matrix and the associated resistance to fractures.

Taken together, these findings suggest that altered lacunae volume and shape distribution are indicative for osteolysis and disease progression from MGUS, SMM to newly diagnosed MM. Future studies are needed to explore whether such changes cause lower local tissue strains and an impaired bone mechanoresponse in MM patients with osteolytic bone lesions and an associated high fracture risk.

Funding

This research was funded by a postdoctoral research fellowship from the Humboldt Foundation (I.M.-J.) and by the Deutsche Forschungsgemeinschaft (DFG) Emmy Noether grant CI 203/2-1 (A.C.). A.C. also thanks the funding from IKERBASQUE Basque Foundation for Science; from the Spanish Ministry of Science and Innovation, grant PID2021-123013OB-I00 funded by MCIN/AEI/10.13039/501100011033/FEDER, UE; from the Fundación Científica Asociación Española Contra el Cáncer (grant number LABAE223466CIIPI) and from Osasun Saila, Eusko Jaurlaritza (grant 2023333027). This work was supported by the Interdisciplinary Center for Clinical Research (IZKF), Medical Faculty of Würzburg, grant B-409 (F.J.) and the German Research Foundation (DFG) grant JU 426/11-1 (F.J., 496963451). E.L. was supported by a grant of the Deutsche Krebshilfe (70112693).

CRedit authorship contribution statement

Inés Moreno-Jiménez: Writing – review & editing, Writing – original draft, Validation, Supervision, Resources, Project administration, Methodology, Investigation, Funding acquisition, Formal analysis, Conceptualization. **Sharen Heinig:** Writing – review & editing, Validation, Software, Methodology, Investigation, Formal analysis. **Unai Heras:** Writing – review & editing, Software, Methodology, Investigation, Formal analysis. **Daniela Simone Maichl:** Writing – review & editing, Investigation. **Susanne Striffler:** Writing – review & editing, Resources, Investigation. **Ellen Leich:** Writing – review & editing, Investigation, Data curation. **Stéphane Blouin:** Writing – review & editing, Investigation. **Peter Fratzl:** Writing – review & editing, Resources. **Nadja Fratzl-Zelman:** Writing – review & editing, Resources. **Franziska Jundt:** Writing – review & editing, Writing – original draft, Validation, Visualization, Supervision, Resources, Project administration, Methodology, Funding acquisition, Conceptualization. **Amaia Cipitria:** Writing – review & editing, Writing – original draft, Validation, Visualization, Supervision, Resources, Project administration, Methodology, Funding acquisition, Conceptualization.

Declaration of competing interest

The authors declare that they have no known competing financial interests or personal relationships that could have appeared to influence the work reported in this paper.

Data availability

The raw/processed data required to reproduce these findings are available in the publicly accessible Edmond repository of the Max Planck Society (<https://doi.org/10.17617/3.5BPJUP>).

Acknowledgements

The authors thank Daniel Werner, Jeannette Steffen, Daniela S. Garske and Susann Weichold at the Max Planck Institute of Colloids and Interfaces in Potsdam for their technical assistance.

Appendix A. Supplementary data

Supplementary data to this article can be found online at <https://doi.org/10.1016/j.bone.2024.117236>.

References

- [1] L.F. Bonewald, The amazing osteocyte, *J. Bone Miner. Res.* 26 (2011) 229–238.
- [2] H. Hemmatian, A.D. Bakker, J. Klein-Nulend, G.H. van Lenthe, Aging, osteocytes, and mechanotransduction, *Curr. Osteoporos. Rep.* 15 (2017) 401–411.
- [3] M. Gerbaix, V. Gnyubkin, D. Farlay, C. Olivier, P. Ammann, G. Courbon, N. Laroche, R. Genthial, H. Follet, F. Peyrin, B. Shenkman, G. Gauquelin-Koch, L. Vico, One-month spaceflight compromises the bone microstructure, tissue-level mechanical properties, osteocyte survival and lacunae volume in mature mice skeletons, *Sci. Rep.* 7 (2017) 2659.
- [4] N.E. Lane, W. Yao, M. Balooch, R.K. Nalla, G. Balooch, S. Habelitz, J.H. Kinney, L. F. Bonewald, Glucocorticoid-treated mice have localized changes in trabecular bone material properties and osteocyte lacunar size that are not observed in placebo-treated or estrogen-deficient mice, *J. Bone Miner. Res.* 21 (2005) 466–476.
- [5] L.M. Tiede-Lewis, S.L. Dallas, Changes in the osteocyte lacunocanalicular network with aging, *Bone* 122 (2019) 101–113.
- [6] S.M. Tommasini, A. Trinward, A.S. Acerbo, F. De Carlo, L.M. Miller, S. Judex, Changes in intracortical microporosities induced by pharmaceutical treatment of osteoporosis as detected by high resolution micro-CT, *Bone* 50 (2012) 596–604.
- [7] M.G. Mullender, D.D. van der Meer, R. Huiskes, P. Lips, Osteocyte density changes in aging and osteoporosis, *Bone* 18 (1996) 109–113.
- [8] S. Blouin, B.M. Misof, M. Mähr, N. Fratzl-Zelman, P. Roschger, S. Lueger, P. Messmer, P. Keplinger, F. Rauch, F.H. Glorieux, A. Berzlanovich, G.M. Gruber, P. C. Brugger, E. Shane, R.R. Recker, J. Zwerina, M.A. Hartmann, Osteocyte lacunae in transiliac bone biopsy samples across life span, *Acta Biomater.* 157 (2023) 275–287.
- [9] P. Milovanovic, E.A. Zimmermann, C. Riedel, A. vom Scheidt, L. Herzog, M. Krause, D. Djonic, M. Djuric, K. Püschel, M. Amling, R.O. Ritchie, B. Busse, Multi-level characterization of human femoral cortices and their underlying osteocyte network reveal trends in quality of young, aged, osteoporotic and antiresorptive-treated bone, *Biomaterials* 45 (2015) 46–55.
- [10] H. Hemmatian, A.D. Bakker, J. Klein-Nulend, G.H. van Lenthe, Alterations in osteocyte lacunar morphology affect local bone tissue strains, *J. Mech. Behav. Biomed. Mater.* 123 (2021) 104730.
- [11] K.G. Yang, E. Goff, K. Io Cheng, G.A. Kuhn, Y. Wang, J.C. yiu Cheng, Y. Qiu, R. Müller, W.Y. wai Lee, Abnormal morphological features of osteocyte lacunae in adolescent idiopathic scoliosis: a large-scale assessment by ultra-high-resolution micro-computed tomography, *Bone* 166 (2023) 116594.
- [12] E.G. Atkinson, J. Delgado-Calle, The emerging role of osteocytes in cancer in bone, *JBM Plus* 3 (2019) e10186.
- [13] M. Adhikari, J. Delgado-Calle, Role of osteocytes in cancer progression in the bone and the associated skeletal disease, *Curr. Osteoporos. Rep.* 19 (2021) 247–255.
- [14] L.C. Hofbauer, A. Bozec, M. Rauner, F. Jakob, S. Perner, K. Pantel, Novel approaches to target the microenvironment of bone metastasis, *Nat. Rev. Clin. Oncol.* 18 (2021) 488–505.
- [15] A.M. Mastro, C.V. Gay, D.R. Welch, H.J. Donahue, J. Jewell, R. Mercer, D. DiGirolamo, E.M. Chislock, K. Guttridge, Breast cancer cells induce osteoblast apoptosis: a possible contributor to bone degradation, *J. Cell. Biochem.* 91 (2004) 265–276.
- [16] H. Hemmatian, S. Conrad, G. Furesi, K. Mletzko, J. Krug, A.V. Faila, J. D. Kuhlmann, M. Rauner, B. Busse, K. Jähn-Rickert, Reorganization of the osteocyte lacuno-canalicular network characteristics in tumor sites of an immunocompetent murine model of osteotropic cancers, *Bone* 152 (2021) 116074.
- [17] G. Roodman, Pathogenesis of myeloma bone disease, *Blood Cells Mol. Dis.* 32 (2004) 290–292.
- [18] J. Berenson, L. Rajdev, M. Broder, Bone complications in multiple myeloma, *Cancer Biol. Ther.* 5 (2006) 1082–1085.
- [19] E. Terpos, I. Ntanasis-Stathopoulos, M.A. Dimopoulos, Myeloma bone disease: from biology findings to treatment approaches, *Blood* 133 (2019) 1534–1539.
- [20] J. Delgado-Calle, J. Anderson, M.D. Cregor, M. Hiasa, J.M. Chirgwin, N. Carlesso, T. Yoneda, K.S. Mohammad, L.I. Plotkin, G.D. Roodman, T. Bellido, Bidirectional notch signaling and osteocyte-derived factors in the bone marrow microenvironment promote tumor cell proliferation and bone destruction in multiple myeloma, *Cancer Res.* 76 (2016) 1089–1100.
- [21] A. Huston, G.D. Roodman, Role of the microenvironment in multiple myeloma bone disease, *Future Oncol.* 2 (2006) 371–378.
- [22] S.V. Rajkumar, M.A. Dimopoulos, A. Palumbo, J. Blade, G. Merlini, M.-V. Mateos, S. Kumar, J. Hillengass, E. Kastiris, P. Richardson, O. Landgren, B. Paiva, A. Dispenzieri, B. Weiss, X. LeLeu, S. Zweegman, S. Lonial, L. Rosinol, E. Zamagni, S. Jagannath, O. Sezer, S.Y. Kristinsson, J. Caers, S.Z. Usmani, J.J. Lahuerta, H. E. Johnsen, M. Beksac, M. Cavo, H. Goldschmidt, E. Terpos, R.A. Kyle, K. C. Anderson, B.G.M. Durie, J.F.S. Miguel, International myeloma working group updated criteria for the diagnosis of multiple myeloma, *Lancet Oncol.* 15 (2014) e538–e548.
- [23] J. Borggrefe, S. Giravent, G. Campbell, F. Thomsen, D. Chang, M. Franke, A. Günther, M. Heller, A. Wulff, Association of osteolytic lesions, bone mineral loss and trabecular sclerosis with prevalent vertebral fractures in patients with multiple myeloma, *Eur. J. Radiol.* 84 (2015) 2269–2274.
- [24] E.M. Lee, B. Kim, Clinical significance of trabecular bone score for prediction of pathologic fracture risk in patients with multiple myeloma, *Osteoporos Sarcopenia* 4 (2018) 73–76.
- [25] M. Takasu, C. Tani, M. Ishikawa, S. Date, J. Horiguchi, M. Kiguchi, A. Tamura, A. Sakai, H. Asaoku, N. Nango, K. Awai, Multiple myeloma: microstructural analysis of lumbar trabecular bones in patients without visible bone lesions—preliminary results, *Radiology* 260 (2011) 472–479.
- [26] M. Michels, K. Morais-Faria, C. Rivera, T.B. Brandão, A.R. Santos-Silva, M. L. Oliveira, Structural complexity of the craniofacial trabecular bone in multiple myeloma assessed by fractal analysis, *Imag. Sci. Dent.* 52 (2022) 33–41.
- [27] F. Ziouti, A.P. Soares, I. Moreno-Jiménez, A. Rack, B. Bogen, A. Cipitria, P. Zaslansky, F. Jundt, An early myeloma bone disease model in skeletally mature mice as a platform for biomaterial characterization of the extracellular matrix, *J. Oncol.* 2020 (2020) 1–12.
- [28] E. Goff, A. Cohen, E. Shane, R.R. Recker, G. Kuhn, R. Müller, Large-scale osteocyte lacunar morphological analysis of transiliac bone in normal and osteoporotic premenopausal women, *Bone* 160 (2022) 116424.
- [29] Y. Carter, C.D.L. Thomas, J.G. Clement, D.M.L. Cooper, Femoral osteocyte lacunar density, volume and morphology in women across the lifespan, *J. Struct. Biol.* 183 (2013) 519–526.
- [30] P.R. Buenzli, N.A. Sims, Quantifying the osteocyte network in the human skeleton, *Bone* 75 (2015) 144–150.
- [31] B.R. McCreddie, S.J. Hollister, M.B. Schaffler, S.A. Goldstein, Osteocyte lacuna size and shape in women with and without osteoporotic fracture, *J. Biomech.* 37 (2004) 563–572.
- [32] E. Gescheidtova, P. Marcon, K. Bartusek, E. Gescheidtová, P. Marcon, K. Bartusek, Visualization of plant fibres via diffusion tensor imaging, in: *PIERS Proceedings, Suzhou, China, 2011*. https://www.researchgate.net/profile/Karel-Bartusek/publication/267556847_Visualization_of_Plant_Fibres_via_Diffusion_Tensor_Imaging/links/5583ec1a08ae89172b861a80/Visualization-of-Plant-Fibres-via-Diffusion-Tensor-Imaging.pdf.
- [33] K.S. Mader, P. Schneider, R. Müller, M. Stapanoni, A quantitative framework for the 3D characterization of the osteocyte lacunar system, *Bone* 57 (2013) 142–154.
- [34] J. Chaumel, M. Schotte, J.J. Bizzarro, P. Zaslansky, P. Fratzl, D. Baum, M.N. Dean, Co-aligned chondrocytes: zonal morphological variation and structured arrangement of cell lacunae in tessellated cartilage, *Bone* 134 (2020) 115264.
- [35] Z.S. Bernstein, E.B. Kim, N. Raj, Bone disease in multiple myeloma: biologic and clinical implications, *Cells* 11 (2022) 2308.
- [36] A. Palumbo, H. Avet-Loiseau, S. Oliva, H.M. Lokhorst, H. Goldschmidt, L. Rosinol, P. Richardson, S. Caltagirone, J.J. Lahuerta, T. Facon, S. Brinthen, F. Gay, M. Attal, R. Passera, A. Spencer, M. Offidani, S. Kumar, P. Musto, S. Lonial, M.T. Petrucci, R. Z. Orlowski, E. Zamagni, G. Morgan, M.A. Dimopoulos, B.G.M. Durie, K. C. Anderson, P. Sonneveld, J. San Miguel, M. Cavo, S.V. Rajkumar, P. Moreau, Revised international staging system for multiple myeloma: a report from International Myeloma Working Group, *J. Clin. Oncol.* 33 (2015) 2863–2869.
- [37] P. Milovanovic, B. Busse, Phenomenon of osteocyte lacunar mineralization: indicator of former osteocyte death and a novel marker of impaired bone quality? *Endocr. Connect.* 9 (2020) R70–R80.
- [38] J. Delgado-Calle, T. Bellido, G.D. Roodman, Role of osteocytes in multiple myeloma bone disease, *Curr. Opin. Support. Palliat. Care* 8 (2014) 407–413.
- [39] R. Schwarzer, N. Nickel, J. Godau, B.M. Willie, G.N. Duda, R. Schwarzer, B. Cirovic, A. Leutz, R. Manz, B. Bogen, B. Dörken, F. Jundt, Notch pathway inhibition controls myeloma bone disease in the murine MOPC315.BM model, *Blood Cancer J.* 4 (2014) e217.
- [40] M. Rummler, F. Ziouti, A.L. Bouchard, A. Brandl, G.N. Duda, B. Bogen, A. Beilhack, M.E. Lynch, F. Jundt, B.M. Willie, Mechanical loading prevents bone destruction and exerts anti-tumor effects in the MOPC315.BM.Luc model of myeloma bone disease, *Acta Biomater.* 119 (2021) 247–258.
- [41] F. Ziouti, M. Rummler, B. Steyn, T. Thiele, A. Seliger, G.N. Duda, B. Bogen, B. M. Willie, F. Jundt, Prevention of bone destruction by mechanical loading is not enhanced by the Bruton's tyrosine kinase inhibitor CC-292 in myeloma bone disease, *Int. J. Mol. Sci.* 22 (2021) 3840.
- [42] E. Tsoardi, K. Jähn, M. Rauner, B. Busse, L.F. Bonewald, Physiological and pathological osteocytic osteolysis, *J. Musculoskelet. Neuronal Interact.* 18 (2018) 292–303.
- [43] K. Jähn, S. Kelkar, H. Zhao, Y. Xie, L.M. Tiede-Lewis, V. Dusevich, S.L. Dallas, L. F. Bonewald, Osteocytes acidify their microenvironment in response to PTHrP in vitro and in lactating mice in vivo, *J. Bone Miner. Res.* 32 (2017) 1761–1772.
- [44] M. Kogawa, A.R. Wijenayaka, R.T. Ormsby, G.P. Thomas, P.H. Anderson, L. F. Bonewald, D.M. Findlay, G.J. Atkins, Sclerostin regulates release of bone mineral by osteocytes by induction of carbonic anhydrase 2, *J. Bone Miner. Res.* 28 (2013) 2436–2448.
- [45] S.Y. Tang, R.-P. Herber, S.P. Ho, T. Alliston, Matrix metalloproteinase-13 is required for osteocytic perilacunar remodeling and maintains bone fracture resistance, *J. Bone Miner. Res.* 27 (2012) 1936–1950.
- [46] V. Schemenz, A. Gjardy, F.F. Chamaseani, A. Roschger, P. Roschger, P. Zaslansky, L. Helfen, M. Burghammer, P. Fratzl, R. Weinkamer, R. Brunner, B.M. Willie, W. Wagermaier, Heterogeneity of the osteocyte lacuno-canalicular network architecture and material characteristics across different tissue types in healing bone, *J. Struct. Biol.* 212 (2020) 107616.